Available online at www.sciencedirect.com

ScienceDirect

Energy Procedia 60 (2014) 3 – 12

Energy Procedia

E-MRS Spring Meeting 2014 Symposium Y "Advanced materials and characterization techniques for solar cells II", 26-30 May 2014, Lille, France

Plasmonic nanoparticle films for solar cell applications fabricated by size-selective aerosol deposition

T.V. Pfeiffer[a], J. Ortiz-Gonzalez[b], R. Santbergen[b]*, H. Tan, A. Schmidt Ott[a], M. Zeman[b], A.H.M. Smets[b]

[a]*Materials for Energy Conversion and Storage, Delft University of Technology, Julianalaan 136, 2628 BL Delft, the Netherlands*
[b]*Photovoltaic Materials and Devices, Delft University of Technology, Mekelweg 4, 2628 CD Delft, the Netherlands*

Abstract

A soft deposition method for incorporating surface plasmon resonant metal nanoparticles within photovoltaic devices was studied. This self-assembly method provides excellent control over both nanoparticle size and surface coverage. Films of spherical Ag nanoparticles with diameter of ~100 nm were fabricated by depositing size-selected aerosols on various substrates using electrophoresis. This novel deposition method opens the route to embed plasmonic nanoparticles in the intermediate reflector of a micromorph silicon tandem PV cell. We have for the first time fabricated working tandem cells of this type. Compared to a flat reference device the Ag particles enhanced the short-circuit current density due to improved light trapping. The enhancement is, however, limited by the sulfidation on the surface of Ag nanoparticles and a further optimization of the cell fabrication method is required to prevent a reduction of open-circuit voltage and fill factor.

Peer-review under responsibility of The European Materials Research Society (E-MRS)

Keywords: light trapping; plasmonics; silver nanoparticles; aerosol; thin-film solar cells.

* Corresponding author. Tel.: +31-15-278-4053; fax: +31-15-278-2968.
E-mail address: r.santbergen@tudelft.nl

Peer-review under responsibility of The European Materials Research Society (E-MRS)
doi:10.1016/j.egypro.2014.12.335

1. Introduction

A film of plasmonic nanoparticles can improve solar cell performance by trapping incident light into the photo-absorbing layer. However, the optical properties of the film depend strongly on the size, shape and surface coverage of the nanoparticles. Ag nanoparticles of ~100 nm diameter are especially attractive due to their large scattering cross sections and relatively low parasitic absorption [1]. Self-assembly methods present advantages over nanofabrication methods for the scalable production of large area nanoparticle films at low cost, as is required for solar cell applications. Metal-island films, formed by annealing a thin metal layer deposited on a substrate, present the most common self-assembly approach. This technique is simple and uses conventional technology. However, to obtain sufficiently large particles and a sufficiently low surface coverage, high annealing temperatures of ~400 °C are required [3]. Particles formed by a lower annealing temperature have a different morphology and suffer from too high parasitic absorption losses [4]. Promising results have been obtained using a plasmonic back reflector in amorphous silicon and micro-crystalline silicon solar cells [5,6]. This back reflector can be fabricated firstly at 400 °C and the thin-film solar cell can be deposited on top afterwards. Embedding the particles inside the intermediate reflector of a micromorph tandem cell would be very interesting as well, as both the forward and backward scattered light can be utilized by top and bottom cell, respectively. However, this would require the formation of the nanoparticles onto an already deposited cell, which limits the processing temperature to ~200 °C.

Exposing the solar cell to high temperatures can be avoided when the silver particles are formed at high temperature separately (i.e. not directly on the substrate) and then deposited onto the solar cell substrate at low temperature. Colloidal routes provide an excellent control of particle size, allowing the formation of ordered nanoparticle layers [7,8]. However, the colloidal suspensions contain large amounts of impurities which are difficult to remove from solar cells, specifically surfactants, and which can seriously deteriorate the performance of thin-film silicon solar cells. Moreover, the surface coverage of nanoparticles is difficult to control. Our objective is to develop a low temperature, low cost, and scalable process to manufacture films of silver nanoparticles with precise control of the size and surface coverage of Ag nanoparticles. Low temperature processing makes it possible to deposit the film directly onto an existing semiconductor layer. To achieve this, we use an aerosol approach that involves the generation of an aerosol of spheroid nanoparticles, isolating particles of a given mobility to obtain a monodisperse particle size, and softly depositing the particles under an electric field [2,9]. In this study, we demonstrate that Ag nanoparticle films of higher purity can be obtained using a spark generator rather than a furnace as the primary aerosol source. We report on the performance of two solar cell configurations: a single junction cell with Ag nanoparticles deposited on micro-crystalline silicon (μc-Si), and a tandem cell with Ag nanoparticles placed between the amorphous silicon (a-Si:H) top cell and μc-Si:H bottom cell.

Nomenclature

d_p	diameter of particle
EQE	external quantum efficiency
FF	fill factor
J_{sc}	short-circuit current density
$Q_{scat.}$	scattering cross-section
$Q_{abs.}$	absorption cross-section
R_s	series resistance
R_{sh}	shunt resistance
V_{oc}	open circuit voltage
η	efficiency
θ	surface coverage
Φ	flow rate at 20°C and 1 atm, in L min^{-1}

2. Experimental methods

2.1. Nanoparticle film deposition

Aerosols of Ag nanospheres at ambient pressure were generated by sintering of agglomerates formed by the evaporation and condensation of silver in a flow of inert gas (Figure 1). The particles were size-selected using a differential mobility analyzer (DMA), and subsequently deposited by electrophoresis in an electrostatic precipitator [2,5]. Silver was evaporated either by heating in a tube furnace [10], or using spark ablation [11]. A Vecstar VTF tube furnace with a 42 cm hot zone was held at 1380 °C. A ceramic boat filled with Ag wire of 99.9 % purity (MaTeck, GmbH) was placed in the middle of the alumina tube. The circuit used in the spark generator is described elsewhere [12]. Sparks were formed between two 4N5 Ag rods of 7 mm diameter (MaTeck, GmbH) with the spark generator running at 1.2 kV and 100 mA. Quench gases at were of 5N0 purity, with flows of 1.8 L min^{-1} N_2 (furnace) and 3.0 L min^{-1} Ar (spark), at 20 °C and 1 atm.

After growing in a 2 L aluminium agglomeration vessel, the particles were reshaped using a second tube furnace (Vecstar VCTF, 100 cm hot zone). A bipolar charge distribution [13] was applied to the sintered particles using a 80 MBq ^{85}Kr β^- source. A Duisburg-type DMA was used size-select the particles. Size-selected nanospheres were deposited on various flat substrates, i.e. glass, glass/TCO and a-Si, in a homebuilt electrostatic precipitator (ESP). The ESP consisted of a 100 mm inner diameter steel vessel, with a grounded, axial 4 mm inner diameter inlet nozzle placed 70 mm above the 40 mm diameter deposition area, with an applied voltage of 7 kV.

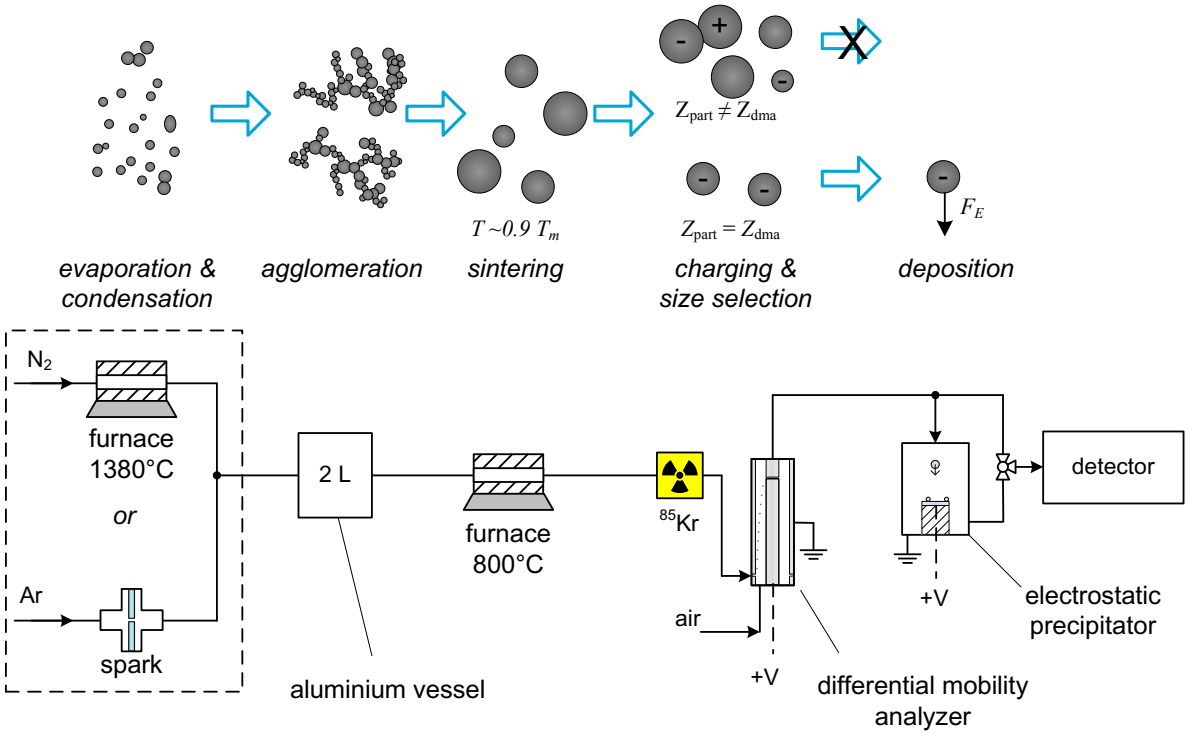

Fig. 1. Process schematic

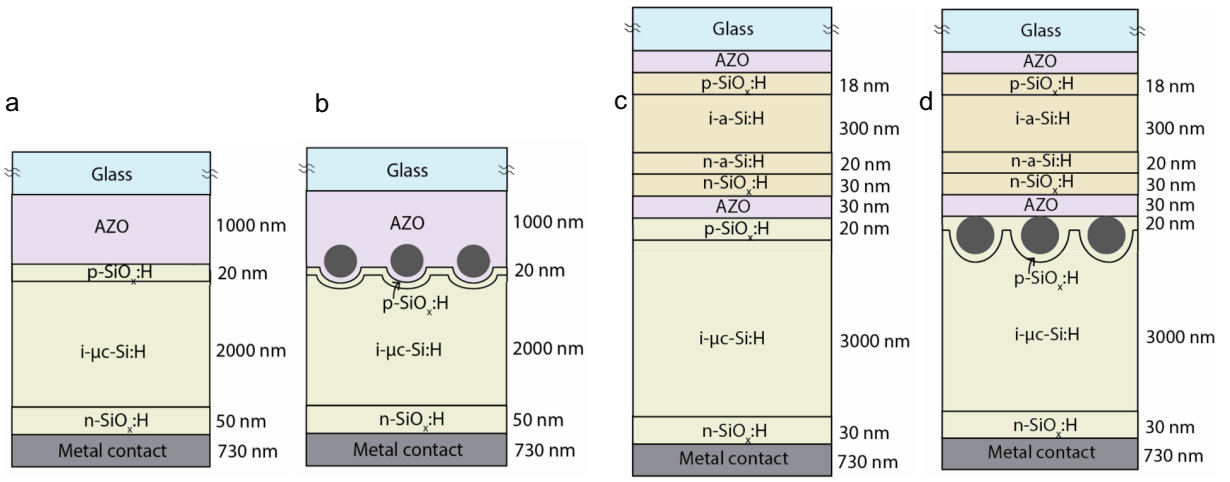

Fig. 2. Configuration of PV cells, (a) single junction reference cell, (b) single junction cell with Ag nanoparticles, (c) micromorph tandem reference cell, and (b) micromorph tandem cell with Ag nanoparticles.

2.2. Solar cell deposition

Arrays of 4*4 mm^2 solar cells were assembled front-to-back on glass substrates. Single-junction and tandem cells both with and without a Ag nanoparticle film were prepared as shown in Figure 2. The Al-doped ZnO (AZO) films were deposited by RF-magnetron sputtering using a ZnO target containing 2%-wt. Al_2O_3. The intrinsic and doped layers of Si were deposited by plasma-enhanced chemical vapour deposition (PECVD). Intrinsic µc-Si:H was deposited at 40.68 MHz (VHF-PECVD); a-Si and doped SiO_x:H at 13.56 MHz (RF-PECVD). The Ag back reflector was deposited by physical vapor deposition (PVD).

In order to deposit the Ag nanoparticle films, the deposited substrates were removed from the vacuum chamber and moved to the aerosol deposition setup shown in Figure 1. The reference cells were subjected to the same vacuum break. In the single junction cells the Ag nanoparticles are located in front of the photo-absorbing layer, embedded in two consecutive AZO layers. In the tandem cells the nanoparticles were deposited on top of the AZO capping layer of the p-i-n a-Si:H top cell. Subsequently, a layer of p-SiO_x:H was deposited directly onto the nanoparticle film, followed by deposition of the rest of the cell.

2.3. Characterization methods

The surface coverage, size and shape of nanoparticles in the Ag films were determined on glass/ITO or on Si wafers using a Hitachi S-4800 scanning electron microscope (SEM). Image analysis was performed using ImageJ software [14]. The investigated area for each sample was >100 μm^2, with particle counts of 250-1500 depending on the surface coverage. Reported diameters are those of projected-area equivalent circles, unless stated otherwise. Elemental compositions were determined by energy dispersive X-ray spectroscopy (EDX) on a JEOL JSM-6010LA, using spot analysis on agglomerates to obtain a sufficient signal.

Absorption and scattering measurements were performed with a Perkin Elmer Lambda 950 spectrophotometer with a 150-mm-diameter integration sphere. JV-curves were recorded under AM1.5G (100 mW cm^{-2}, Oriel Newport). Mieplot v4.3 [15] was used to calculate scattering and absorption cross-sections of Ag nanoparticles according to the Mie theory. Cross-sections were averaged over the particle size distributions obtained from the SEM measurements. The Matlab package MatScat [16] was used to simulate the scattering of Ag-Ag_2S core-shell particles. Optical constants for Ag [17] and Ag_2S [18] were obtained from literature.

3. Results and discussion

3.1. Deposition of Ag nanoparticle films

SEM micrographs reveal that the Ag nanoparticles are deposited randomly over the substrate surface (Figure 3). With the furnace as primary aerosol source, the surface coverage grows at a constant rate of 2.4% h^{-1} from 2.3% after 50 min (Figure 3a) to 10.8% after 270 min deposition (Figure 3c). As the film grows, the mode of the particle size distribution does not shift to larger sizes, indicating that the primary particle size of 107 nm stays constant (Figure 3d). Instead, doublets and triplets form as multiple particles deposit on the same site, resulting in a larger fraction of >150 nm particles. This surface agglomeration limits the maximum attainable surface coverage to 5%-10 %. As the particles leaving the DMA all have the same polarity, electrostatic repulsion could be used to reduce agglomeration at high surface coverage. Simulations following Krinke's method [19] show that each particle would need to carry an impractical four charges –and not dissipate the charge upon deposition– in order for this effect to be usable at this particle size.

Films produced by spark discharge show similar spherical particles and aggregates (Figure 4). The difference in mode between Figures 3 and 4 results from a change in the DMA settings; the particles are still size-selected, but for a smaller size. A notable number of agglomerates, i.e. non-sintered particle clusters, comprises round spheres with diameters <60 nm (Figure 4b). Unlike multiply charged doublets and triplets, these small particles cannot have passed the mobility-based size selection independently. As they are spheres, they must have agglomerated by coagulation after the sintering furnace, but before the DMA. The agglomeration rate of an aerosol is proportional to the concentration squared (N^2) [20], and we conclude that the spark-generated aerosol had a higher concentration than that generated by furnace. The coagulation effect can be avoided by placing the DMA before the sintering furnace, as done by Harra et al. [9]. In cases where a high degree of monodispersity is needed, two DMA's can be used in series.

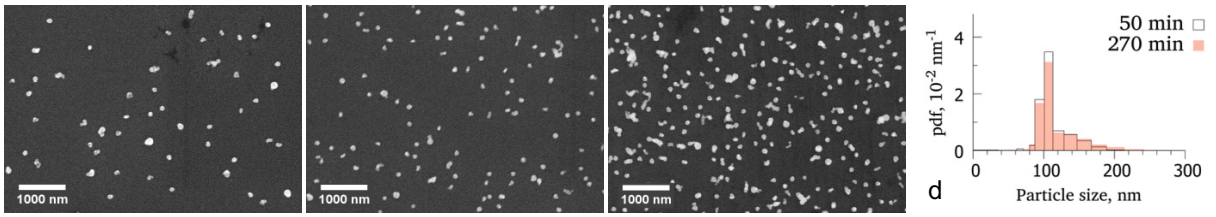

Fig. 3. SEM micrographs of furnace-generated, size-selected particles on Si, deposited for (a) 50 min, (b) 90 min, and (c) 270 min. (d) Size distribution function for 50 and 270 min deposition.

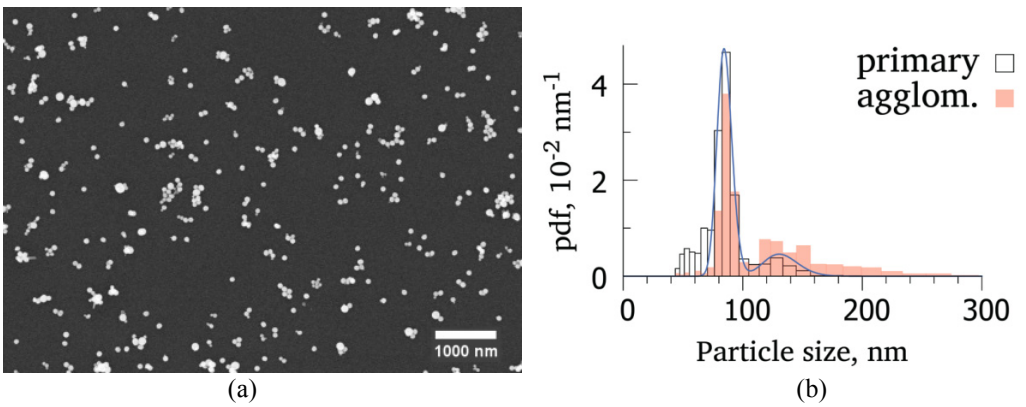

Fig. 4 Spark-generated, size-selected particles deposited on Si, (a) SEM micrograph, (b) particle size distribution function.

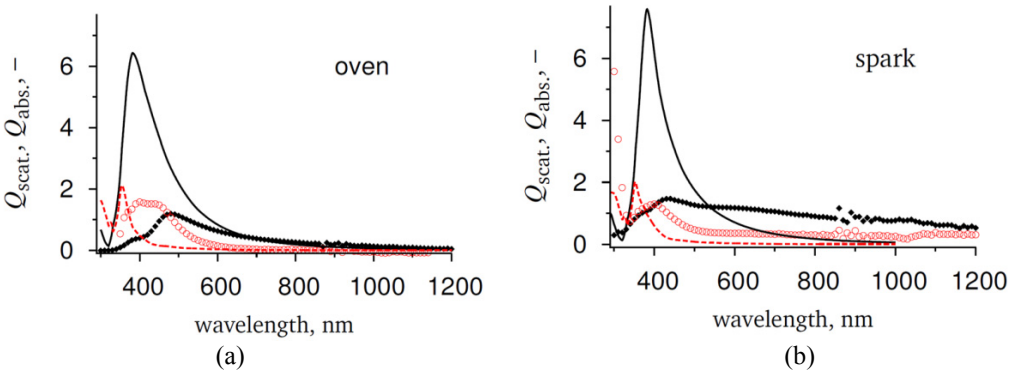

Fig. 5 Measured (points) and simulated (lines) cross-sections for scattering (black) and absorption (red). (a) tube furnace, d_p = 107 nm, θ = 10 %. (b) spark discharge, d_p = 84 nm, θ = 10 %.

3.2. Characterization of nanoparticle films

Nanoparticle films with particle size of 107 nm and surface coverage of 10% deposited onto TCO coated glass substrates were characterized optically. Total and diffuse reflectance (R_{tot} and R_{dif}) and transmittance (T_{tot} and T_{dif}) of both the nanoparticle samples and of the bare substrates were measured in the wavelength range 300 to 1200 nm. From these measurements the absorbance $A = 1\text{-}R_{tot}\text{-}T_{tot}$ and the scattering $S = R_{dif} + T_{dif}$ of the samples were determined. By subtracting the value of the bare substrate from the value of the sample with nanoparticles, the absorbance and scattering due to the nanoparticles were obtained. By dividing the nanoparticle absorbance and scattering by the surface coverage, the absorption efficiency Q_{abs} and scatter efficiency Q_{scat} were obtained. In Figure 5 the results are shown and compared to Mie theory. The measured $Q_{scat.}$ and $Q_{abs.}$ show the surface plasmon resonance (SPR), however at a much lower magnitude than the scatter cross-section. The measured SPRs show a red shift, which is smaller for the spark-generated particles ($Q_{scat.}$= 60 nm, $Q_{abs.}$= 50 nm), than for furnace-generated samples ($Q_{scat.}$= 90 nm, $Q_{abs.}$= 80 nm). Three causes can be identified for the deviation from Mie theory: (1) the simulations assume the particle is embedded in a medium of known refractive index, while the particles are deposited on the interface between two media, (2) the particles are not ideal spheres, and (3) impurities in the Ag particles modify its optical constants. A more rigorous model can remove the uncertainty in the medium's refractive index, or the particles could be fully embedded, e.g. in a TCO. The sphericity of the particles can be increased by modifying the conditions in the sintering furnace [9]. The contaminants should be avoided completely, if possible.

EDX was performed on Ag nanoparticles deposited on silicon wafer to identify the source of contamination (Table 1). Both particle sources show a different contaminant profile. The furnace contaminants originate from the alumina work tube of the furnace, which, despite thorough cleaning, clearly contained the volatile NaCl. Volatile contaminants, even if present in trace quantities, leech from the tube walls in sizeable fluxes due to their high vapor pressure at the operating temperature, and the large heated surface area of the tube (~300 cm^2) [21]. Following the Clausius-Clapeyron equation, the vapor pressure increases exponentially with temperature. The sintering furnace, operated at much lower temperature, is thus expected to give significantly lower contamination levels, as evidenced by the lower contamination levels in spark-generated particles. The heated surface area in the spark is <1 cm^2 and comprises only the target electrode, so that only impurities already present in the electrode can co-evaporate.

Sulfur is the main contaminant for spark-generated particles. It is likely present as Ag_2S, which is known to form when silver is exposed to ambient air [22,23]. A sulfide shell as thin as 1 nm causes a sizeable red shift and decrease in magnitude of the surface plasmon resonance [24]. With growth rates up to 10 nm/h [22], this means that even a short air-exposure will cause a large reduction in scatter cross-section. From the scattering and absorption data (Figure 6, absorption not shown) of simulations of core-shell Ag/Ag_2S (Figure 6(a)) and optical measurements after different exposure times (Figure 6(b)), we estimate an Ag_2S thickness of ~3 nm after overnight air exposure, and

Table 1. Molar composition of air-exposed Ag nanoparticle films, determined by EDX. C and Si are excluded in the calculations due to their strong background signal. *Samples containing oxygen also show elevated carbon levels.

Element	Furnace	Spark
Ag	51–73%	84–87%
Na	0–7%	0–1%
Cl	11–34%	1–2%
S	0–3%	10–12%
O*	13–23%	0-1%
Al	0–1%	0%
Mg, K, Ca and Cu	0–1%	n.d.

~7 nm after 24 days. This is consistent with the EDX data, recorded after 260 days air-exposure, from which a shell thickness of 9-12 nm is calculated. The low sulfidation of the furnace-generated particles suggests that the other contaminants, likely the stable AgCl, protect against sulfidation, although the SPR of Ag remains weakened.

3.3. Results of plasmonic solar cells

3.3.1. Single junction microcrystalline-Si solar cells

Silver nanoparticles with a diameter of 104 nm and 120 nm and a surface coverage of ~10% were deposited on TCO-coated glass. Microcrystalline silicon solar cells with an intrinsic layer thickness of 2 µm were deposited front to back on this substrate, and for reference on a similar substrate without particles. The incorporation of an Ag nanoparticle layer in the front AZO layer increased the short circuit current density by 4-15% (Table 2). Enhanced light absorption is evidenced by an increased EQE above 600 nm (Figure 7a). The surface plasmon resonance will be red shifted and broadened in comparison to the uncovered films due to the change in refractive index of the medium (n_{air} ~ 1 vs. n_{AZO} ~ 2). In the 400-600 nm range the EQE of the cell with 120 nm particles is enhanced, which might be due to an anti-reflection effect. The fact that this is effect is not present for the sample with 104 nm particles is an indication that the anti-reflection effect may not be caused by the plasmonic nanoparticles. The variation in EQE (±7%, not shown) of the individual dots in cell C suggests that the enhancement below 600 nm is linked to inhomogeneous deposition of the front TCO, and not caused by any plasmonic effects.

The scattering nanoparticle film yields an enhanced short circuit current density J_{sc} (Figure 7b). However, efficiency is offset by a decrease in both V_{oc} and fill factor, indicating the increased recombination of charge carriers as a result of electrical defects associated with the Ag nanoparticle layer. SEM measurements revealed the presence of micrometer sized particles, identified as agglomerates of Ag nanoparticles and ambient dusts accrued during

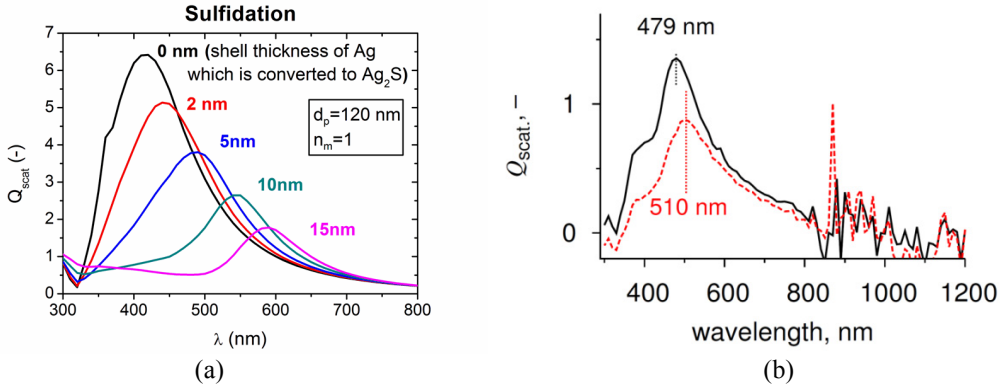

Fig. 6. (a) Simulated scattering cross-sections of Ag/Ag_2S core-shell particles, d_p = 120 nm. (b) Scattering cross-section of 136 nm furnace-generated Ag particles deposited on glass/ITO, measured 1 day (black, solid lines) and 24 days (red, dashed) after deposition.

Table 2. Summary of solar cell parameters for single junction µc-Si:H solar cells.

Parameter	Single junction		
	A (Reference)	B	C
Particle size d_p, nm	n.a.	104	120
Open circuit voltage V_{oc}, mV	541	518	511
Short-circuit current density J_{sc}, mA cm^{-2}	18.3	19.8	20.9
Fill factor FF, %	69.0	61.3	60.7
Efficiency η, %	6.9	6.5	6.8
Series resistance R_S, Ω cm^2	3.1	2.6	3.9
Shunt resistance R_{SH}, Ω cm^2	293	133	243

sample transfer outside of the clean room. These microparticles present a surface roughness that can result in non-conformal coating, voids and pinhole defects [25], contributing to the low R_{SH} (Table 2). Considering that the deposited Si film was only 2 µm thick, such micrometer sized particles by themselves can present direct shunt paths in the cell.

3.3.2. a-Si:H/µc-Si:H Tandem Solar Cells

The a-Si:H/µc-Si:H tandem solar cells were deposited front to back on a glass TCO substrate. The a-Si:H top cell was deposited first and silver nanoparticles with a diameter of 96 nm were deposited on top. Finally the µc-Si:H bottom cell was deposited directly on top of the nanoparticles (see Figure 2c-d).

EQE measurements under bias light were preformed to compare the photocurrent contributions for top and bottom cells to the values of the flat reference device (Figure 8). The silver nanoparticles increase the EQE of the bottom cell in the 800-1000 nm range. A lower reflectance of the solar cells measured in this range indicates that the enhancement is a result of improved light trapping. However, the EQE of the top cell is reduced over the entire wavelength range. An EQE measurement without applied bias light (not shown) revealed that the top cell is shunted and this is the most likely cause of the reduced EQE. Although the exact mechanism is not clear, the shunts are probably induced during deposition of nanoparticles on the already deposited top cells. Annealing at 150°C passivates some of the defects, improving the fill factor of the tandem cell (Figure 9). However, as with the single junction cells, the nanoparticle film does not lead to an increase in solar cell efficiency.

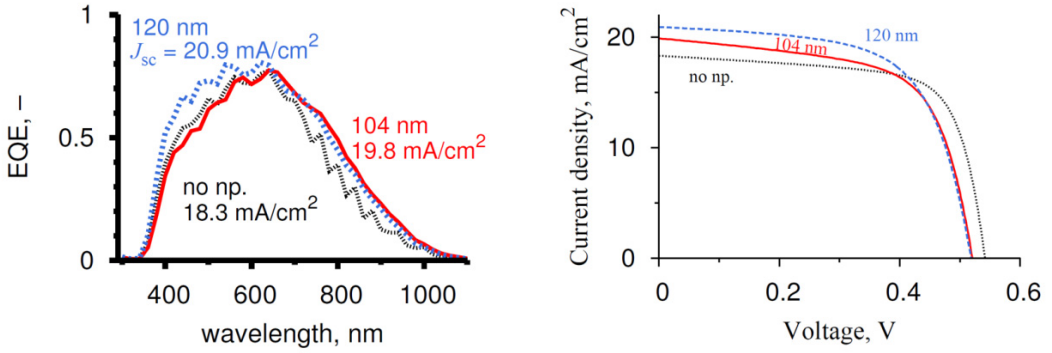

Fig. 7. Characterization of single junction cells. (a) EQE vs wavelength (b) *JV*-curves. *Black:* reference, *red:* 104 nm Ag, *blue dotted:* 120 nm

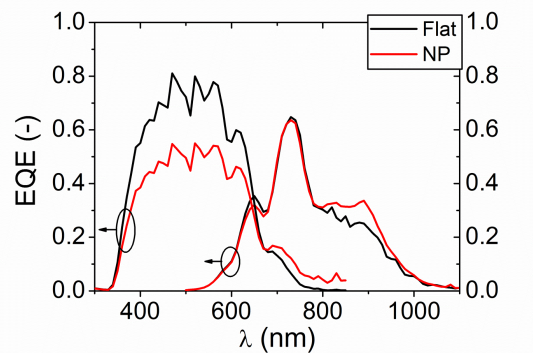

Fig. 8. EQE measurements at Vbias = 0 V under bias light of 870 nm (measures top cell) and 370 nm (bottom cell).

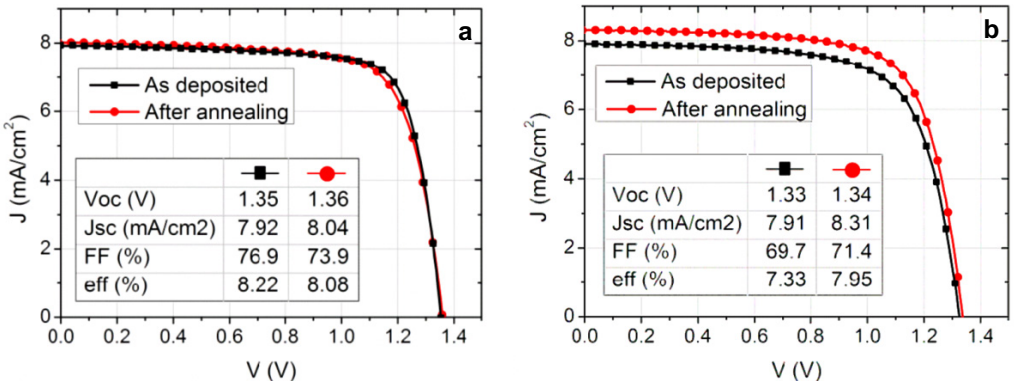

Fig. 9. *JV*-curves of tandem cells. (a) reference cell (b) cell with 96 nm Ag nanoparticles.

4. Conclusion

The presented Ag nanoparticle thin films represent a low temperature alternative to metal-island films, allowing greater flexibility in plasmonic solar cell design. Particle size and polydispersity are controlled through the DMA parameters. Surface coverage is controlled through deposition time. Surface agglomeration starts to become an issue when the surface coverage approaches ~10%. To reduce agglomeration at high aerosol concentrations, a DMA should be placed before the sintering oven. The measured scatter cross sections of the nanoparticles are about 5 times lower than predicted by Mie theory simulations for a pure silver particle as a result of impurities. The high levels of impurities in furnace-generated particles are avoided if spark ablation is used. To avoid the formation of Ag_2S air-exposure must be avoided, preferably by integrating the aerosol deposition system into the vacuum workflow.

Both single junction and tandem solar cells were fabricated. The forward scattered light from the Ag nanoparticle films increases the EQE of underlying μc-Si cells through light-trapping. However, the overall performance of the cells is reduced by the Ag nanoparticles because of a reduced electrical performance. Defects resulting from growing the Si layers on the textured surface of the nanoparticle films can partially be reduced by annealing. Further study on a method of depositing a defect-free (intermediate) layer on the nanoparticle film is required.

Acknowledgements

This work has been funded by the Dutch STW Vidi grant-10782 of A. Smets. TP acknowledges financial support from Agentschap.nl under grant EOT-LT 07052.

References

[1] Atwater HA, Polman A. Plasmonics for improved photovoltaic devices. Nat Mater 2010;9:205–13.
[2] Santbergen R, Tan H, Pfeiffer T, Li X, Frijnts T, Smets A, et al. Plasmonic Solar Cells with Embedded Silver Nanoparticles from Vapor Condensation. MRS Online Proc Libr 2012;1391:mrsf11–1391–j06–07.
[3] Tan H, Santbergen R, Smets AHM, Zeman M. Plasmonic Light Trapping in Thin-film Silicon Solar Cells with Improved Self-Assembled Silver Nanoparticles. Nano Lett 2012;12:4070–6.
[4] Santbergen R, Temple TL, Liang R, Smets AHM, Swaaij RACMM van, Zeman M. Application of plasmonic silver island films in thin-film silicon solar cells. J Opt 2012;14:024010.
[5] Tan H, Sivec L, Yan B, Santbergen R, Zeman M, Smets AHM. Improved light trapping in microcrystalline silicon solar cells by plasmonic back reflector with broad angular scattering and low parasitic absorption. Appl Phys Lett 2013;102:153902.
[6] Tan H, Psomadaki E, Isabella O, Fischer M, Babal P, Vasudevan R, et al. Micro-textures for efficient light trapping and improved electrical performance in thin-film nanocrystalline silicon solar cells. Appl Phys Lett 2013;103:173905.
[7] Derkacs D, Lim SH, Matheu P, Mar W, Yu ET. Improved performance of amorphous silicon solar cells via scattering from surface plasmon polaritons in nearby metallic nanoparticles. Appl Phys Lett 2006;89:093103.
[8] He S, Yao J, Jiang P, Shi D, Zhang H, Xie S, et al. Formation of Silver Nanoparticles and Self-Assembled Two-Dimensional Ordered Superlattice. Langmuir 2001;17:1571–5.
[9] Harra J, Mäkitalo J, Siikanen R, Virkki M, Genty G, Kobayashi T, et al. Size-controlled aerosol synthesis of silver nanoparticles for plasmonic materials. J Nanoparticle Res 2012;14:1–10.
[10] Scheibel HG, Porstendörfer J. Generation of monodisperse Ag- and NaCl-aerosols with particle diameters between 2 and 300 nm. J Aerosol Sci 1983;14:113–26.
[11] Schwyn S, Garwin E, Schmidt-Ott A. Aerosol generation by spark discharge. J Aerosol Sci 1988;19:639–42.
[12] Pfeiffer TV, Feng J, Schmidt-Ott A. New developments in spark production of nanoparticles. Adv Powder Technol 2014;25:56–70.
[13] Wiedensohler A, Fissan HJ. Bipolar Charge Distributions of Aerosol Particles in High-Purity Argon and Nitrogen. Aerosol Sci Technol 1991;14:358–64.
[14] Schneider CA, Rasband WS, Eliceiri KW. NIH Image to ImageJ: 25 years of image analysis. Nat Methods 2012;9:671–5.
[15] Laven P. MiePlot: A computer program for scattering of light from a sphere using Mie theory & the Debye series 2014.
[16] Schäfer J-P. Implementierung und Anwendung analytischer und numerischer Verfahren zur Lösung der Maxwellgleichungen für die Untersuchung der Lichtausbreitung in biologischem Gewebe. Ulm University, 2011.
[17] Johnson PB, Christy RW. Optical Constants of the Noble Metals. Phys Rev B 1972;6:4370–9.
[18] Bennett JM, Stanford JL, Ashley EJ. Optical Constants of Silver Sulfide Tarnish Films. J Opt Soc Am 1970;60:224–31.
[19] Krinke TJ, Deppert K, Magnusson MH, Schmidt F, Fissan H. Microscopic aspects of the deposition of nanoparticles from the gas phase. J Aerosol Sci 2002;33:1341–59.
[20] Hinds WC. Aerosol Technology: Properties, Behavior, and Measurement of Airborne Particles. 2nd ed. Wiley-Interscience; 1999.
[21] Peineke C, Attoui MB, Schmidt-Ott A. Using a glowing wire generator for production of charged, uniformly sized nanoparticles at high concentrations. J Aerosol Sci 2006;37:1651–61.
[22] Bennett HE. Formation and Growth of Tarnish on Evaporated Silver Films. J Appl Phys 1969;40:3351.
[23] Franey JP, Kammlott GW, Graedel TE. The corrosion of silver by atmospheric sulfurous gases. Corros Sci 1985;25:133–43.
[24] McMahon MD, Lopez R, Meyer III HM, Feldman LC, Haglund Jr. RF. Rapid tarnishing of silver nanoparticles in ambient laboratory air. Appl Phys B 2005;80:915–21.
[25] Li HBT, Franken RH, Rath JK, Schropp REI. Structural defects caused by a rough substrate and their influence on the performance of hydrogenated nano-crystalline silicon n–i–p solar cells. Sol Energy Mater Sol Cells 2009;93:338–49.